Green synthesis of copper iodide nanoparticles: gamma irradiation for spectroscopic sensing of cancer biomarker CA 19-9

Shalmali Basu[1] · Debashree Das[1] · David Morgan[2] · Bibhas Hazra[3] · Abhijit Saha[4] · Kamalika Sen[1]

Abstract
A simple, fast, green and cost-effective method is designed for the synthesis of copper iodide nanoparticles (CuI-NP) for spectroscopic detection of cancer biomarker, carbohydrate antigen 19-9 (CA 19-9). Results of UV-visible spectroscopy establish the efficacy of prepared CuI-NP to sense CA 19-9 in serum medium even at its low concentration (~0.066 U/mL). Our study reveals that γ-irradiated (24 h) copper iodide nanoparticles (CuI-NP-γ) have higher sensitivity towards CA 19-9 sensing due to their higher surface activity and charged nature as compared to CuI-NP. CuI-NP-γ could deliver higher signal enhancement and was able to lower the limit of detection (LOD) of CA 19-9 from 0.082 to 0.066 U/mL. Results also indicate that in presence of high concentration of glucose, cholesterol, bilirubin and insulin, which cause pathophysiological disorders like diabetes, hypercholesterolemia, hepatic disorder, hyperinsulinemia, etc., the LOD is even lower (0.037, 0.034, 0.157, 0.029 U/mL respectively). The interaction between the biomarker and the NPs were further established using fluorescence and circular dichroism spectroscopy. The specificity of sensing was tested by checking the response in presence of other biomarkers, like CEA and CA-125 which did not show any signal enhancement with CuI-NP-γ.

Keywords Copper iodide nanoparticles · Green synthesis · γ-Irradiation · Carbohydrate antigen 19-9 · Cancer biomarker · Sensing

Introduction

Pancreatic cancer has become a global problem as it is ranked as 4th major cause of cancer death due to its extremely poor prognosis and high mortality rate [1, 2]. Carbohydrate antigen 19-9 (CA 19-9), the sialyl derivative of Lewis antigen, is considered as gold standard for early diagnosis, prognosis, monitoring and treatment of pancreatic cancer [3–5]. The elevated level of CA 19-9 (>37 U/mL) is also associated with other cancers like breast, bile, ovarian, lungs, etc., and with some non-cancerous pathological disorders like inflammation in bile, jaundice or pancreatitis [6–8]. Hence early and ultra-sensitive detection of CA 19-9 with high specificity and selectivity would be favorable for better disease management and increase in survival rate of the patients. Several methods are already reported for the detection of CA 19-9 including chromatography, enzyme linked immunosorbent assays (ELISA), photoelectrochemical immunoassays, immunofluorescence, etc. [9, 10]. These techniques are usually multi-step and time-consuming processes as labeling and extensive sample preparations are required before the detection, which may result in erroneous information due to interference of the labeling materials in the targeted binding sites. Moreover, cost effective antibody- free methods with ultra-sensitivity are still in demand due to high production cost, batch to batch variation, poor stabil- ity and long incubation time of the conventional methods. Unlike electrochemical sensors, detection of biomarkers based on spectroscopic methods makes the biosensors more cost effective. Hence improvements are still needed in devel- oping biosensors based on optical spectroscopic approach to

✉ Kamalika Sen
kamalchem.roy@gmail.com; kschem@caluniv.ac.in

[1] Department of Chemistry, University of Calcutta, 92, APC Road, Kolkata 700009, India

[2] Cardiff Catalysis Institute, School of Chemistry, Cardiff University, Park Place, Cardiff CF10 3AT, UK

[3] Department of Chemical Sciences, Indian Institute of Science Education and Research (IISER) Kolkata, Mohanpur, Nadia, West Bengal 741246, India

[4] UGC-DAE Consortium for Scientific Research, Kolkata Centre, III/LB-8, Bidhannagar, Kolkata 700098, India

minimize the cost and to achieve highly accurate and ultra-sensitive detection of CA 19-9.

The amalgamation of nanotechnology and biology holds the superior potential to modernize health care and medical diagnostic field as it can address ample biomedical issues using an environmentally-benign technology [11]. Nano- sized materials are often considered as powerful analytical tools for medical diagnostics and treatments, biomedical imaging, screening, sensing, targeted drug delivery and gene delivery systems, etc. [11–13]. Nanoparticles (NPs) possess multi-functionality as they have several exceptional features like small size, size-dependent quantum confinement effects, high surface area and surface charge. They also exhibit good solubility and surface chemistry, decent optical, electrical, thermal, magnetic, catalytic properties, etc., and thus are often used for sensing biomolecules for their multiplexing and miniaturization capabilities [14, 15].

Recently copper iodide nanoparticles (CuI-NP) have gained attention due to their unique photophysical properties like higher band gap, diamagnetic behavior, etc. [16]. Hence applications of CuI-NP as p-type semiconductor, catalysts, in solid state solar cells are widely established [17–21]. Besides their optical and electrical properties, recently it was established that CuI-NP possess high medicinal values due to their antimicrobial properties [22, 23]. However, the potential applications of these nanoparticles as biosensors for the detection of cancer biomarkers are still not established.

In literature, several methods for synthesis of CuI-NP including chemical, hydrothermal, pulse laser deposition, vacuum evaporation, electrochemical, and others have been reported earlier [24–28]. However, as these methods raise environmental concerns over the years, employment of green chemistry driven methods for the synthesis of CuI-NP has recently drawn attention of the researchers due to their eco- logical and economical compatibilities [29]. Nature has an abundant source of bio-reagents present in the form of its wide-ranging variety of plants, microorganisms, etc. [29]. Use of phytochemicals, which are found in different parts of plants like fruit, seed, skin, leaf, flower, bark, etc., acting as reducing and stabilizing agents are more sustainable as com- pared to the use of inorganic ones due to their low cost, easy availability, simpler synthetic steps, higher efficiency and involvement of non-toxic solvent medium [30]. These phyto- chemicals contain hydroxyl, phenolic and carboxylic groups, which act as stabilizing, reducing and capping agents that offer an added advantage over the chemical reducing agents for the controlled growth of the nanoparticles [31, 32]. Recent studies have shown the synthesis of CuI-NP using different green techniques. Archana et al., have synthesized CuI-NP using *Hibiscus rosa-sinensis* L. flower extract [33]. The main polyphenols present there are anthocyanin and cyanidin-3-sophoroside which act as reducing and capping agents. Similarly, green synthesis of CuI-NP was achieved using the extract of red cabbage which has some antibacterial properties [23] and with another widely available polyphenol gallic acid for the formulation of PVA liquid bandages [32] . Again, *Syzygium cumini* seed extract was prepared to synthesize CuI nanoflowers [34]. CuI-NP produced in this way has high surface area with some crystal defects which make it a suitable candidate for adsorption of Cr(VI) and Mn(VII). Kidney bean seed extract has also been used for CuI-NP synthesis [22]. CuI nanocrystalline materials has been synthesized by using the pomegranate juice at ambient temperature [31]. By varying the amount of pomegranate juice, morphology of CuI nanostructure seems to change due to the change in concentration of the anthocyanin which is the primary polyphenol present in pomegranate juice. Cotton textile fibers (commercial cellulose) were also used for CuI-NP synthesis which is an efficient and scalable technique [35]. Morin, a naturally occurring plant polyphenol generally found in several fruits and vegetables like *Psidium guajava, Maclura pomifera, Maclura tinctoria*, has earlier been used in the synthesis of Ru-NP [36]. It has anti-oxidant, anti-inflammatory, anti-neoplastic, chemopre- ventive, cardioprotective properties and has the metal ion chelating capacities [37].

Gamma irradiation is considered as one of the green, safe, and efficient routes for the synthesis and modification of metal-nanoparticles [29, 30, 36]. It can modify the physico-chemical properties of the nanoparticles and can enhance the chemical reactivities on their surfaces [36, 38]. Gamma irra- diation generates free electrons (e^-_{aq}) and free radicals (H• and OH•) in aqueous solutions which facilitates uniform reduction of the bulk metal ions to their nano-state [29, 30, 36, 38, 39]. This method is simple, clean, free from impuri- ties and make the nanoparticles eligible for their electrical, optical and sensing properties [29, 40]. By controlling the radiation dose, strength and time, particle size of the nano- particles and their properties can also be fine-tuned [29, 36, 38]. This high energy beam can change the physicochemical properties of the nanoparticles by creating lattice defects, cluster defects and dislocations [38] and cause lattice strain as well as enhance magnetic properties of nanoparticles like Ag-NP [30]. Gamma irradiation produces radiolysis products of water that generate more charge on the surface of the nanoparticles, viz., Ru-NP has shown selective lan- thanoid sensing of Ce(III), Ce(IV), Dy(III) [36], Fe-NP has shown sensing of perchlorate ions [39]. Conditions for radia- tion seem to play a major role in deciding the size, shape, yield and distribution of several nanoparticless like Au-NP, Ru-NP, ZnO-NP, etc. [29, 36, 41].

In our present work, we aim to synthesize gamma irradiated CuI-NP using green approach with a naturally occurring antioxidant, morin hydrate. This yellow-colored crystalline polyphenol is found to exhibit anticancer activities towards

several cancer cell lines including lung cancer, colon cancer, breast cancer, etc. [42–45]. Herein, we aim to develop a fast and cost-effective green method for the synthesis of CuI-NP followed by gamma irradiation for surface activation. These modified CuI-NPs were found to be able in sensing cancer biomarker CA 19-9 with a significantly low detection limit. The method can be followed to detect pancreatic cancer at an early stage in order to reduce its fatality rate. The gamma irradiated CuI-NP for the optical sensing of biomarkers has revealed their potential in developing a new field in medical diagnostics for biomarker detection. Moreover, this study is a novel approach for the detection of CA 19-9 in presence of several common physiological parameters also.

Materials and methods

Materials

Copper sulphate, potassium iodide and dextrose were obtained from Merck, India. Morin hydrate was purchased from Sigma-Aldrich, India. Carbohydrate antigen 19-9 (CA 19-9) was procured from Monobind Inc., USA. Ringer-Lactate solution (RL) (aqueous solution of sodium lactate, sodium chloride, potassium chloride, calcium chloride) and semisynthetic human insulin actrapid and huminsulin were obtained from local pharmacy. Cholesterol was purchased from LOBA Chemie. Bilirubin was purchased from HiMedia, India. Commercial reference material Lyphochek Assayed Chemistry Control (Bio-Rad) was used as lyophilized human serum-based control and serum solution was reconstituted by following the provided literature. Triple distilled water was used throughout the experiments.

Instruments

For gamma irradiation, a radiation chamber GC 5000 (obtained from BRIT, India) with ^{60}Co source of strength 3.7 kCi with a cylindrical sample chamber (diame- ter of 10.6 cm and height of 14.2 cm) was used. The UV-Vis- ible spectra were obtained using a Hitachi UV–Vis U-3501 spectrophotometer and a Perkin Elmer LS-55 fluorescence spectrometer was used to perform fluorescence spectroscopy with a quartz cuvette having path length 1 cm. A JEOL JEM-2100 F transmission electron microscope (TEM) with 200 kV electron source was used to record the micrographs and selected area electron diffraction (SAED) patterns of the synthesized nanoparticles. Dynamic light scattering (DLS) experiment was performed using a Malvern Zetasizer Nano ZS instrument. Rigaku Smart Lab automatic high resolution multipurpose PC Controlled X-Ray diffractometer system was used to perform powder X-ray diffraction (PXRD) analysis. Fourier Transform Infrared (FTIR) spectroscopic data were recorded using a Perkin Elmer FTIR/FIR spectrometer (Frontier). X-ray photoelectron spectroscopy (XPS) was performed using a Kratos Axis Ultra DLD photoelectron spectrometer, using a monochromatic Al K-α X-ray source operating at 120 W (10 mA × 12 kV). Data were collected with pass energies of 160 eV for survey spectra, and 40 eV for the high-resolution scans with step sizes of 1 eV and 0.1 eV respectively. The system was operated in the Hybrid mode, using a combination of magnetic immersion and electrostatic lenses, and acquired over an area of approximately 300 × 700 μm^2. A magnetically confined charge compensa- tion system using low energy electrons was used to minimize charging of the sample surface, and all spectra were taken with a 90° take off angle. A pressure of ca. 3×10^{-9} Torr was maintained during collection of the spectra. The data were analyzed using Casa XPS (v2.3.24) [46] after subtraction of a Shirley background and using modified Wagner sensitiv- ity factors as supplied by the instrument manufacturer. Data were calibrated to the lowest C1s peak taken to be 285 eV and the binding energies are quoted with an uncertainty of ±0.2 eV. Where applicable, data were fitted using an asymmetric Lorentzian, Voigt like function (LA Lineshape in Casa XPS). Circular dichroism spectroscopy (CD) was performed using Jasco J1100 model. To sonicate the nanoparticle solutions, a Labman digital ultrasonic cleaner (model: LMUC-2) was used and a Remi Elektrotechnik Ltd R-4 C centrifuge was used for centrifugation purposes.

Synthesis of CuI nanoparticles

A simple, environment friendly and cost-effective method was applied for the synthesis of the CuI nanoparticles. Here, plant derived natural polyphenol morin hydrate is used as a reducing agent as well as a stabilizing agent instead of hazardous and/or costly chemicals. 50 mL of 5 mM $CuSO_4{\cdot}5H_2O$ was taken in a beaker and ethanolic solution of morin hydrate (7.5 mg in 1 mL) was added to it under stirring condition. To this, 50 mL of 5 mM KI was added in a dropwise manner. After 2 h of stirring, the solution mixture was kept to settle at room temperature (25 ± 1 °C). The solution turns yellowish along with the formation of brown particles in the solution. A similar solution mixture was prepared and stirred for 2 h and then subjected to gamma irradiation (dose rate 1.27 kGy/h) for 24 h. Upon gamma irradiation, the particles changed their colour from brown to off-white in the solution. Interestingly, there is a glittery appearance in the γ-irradiated off-white particles in the solu- tion. Both the solution sets were then dried under IR lamp to get the desired nanoparticles. While the non-irradiated parti- cles change their colour from brown to black during drying under IR lamp, γ-irradiated (24 h) particles retain their col- our. Both the types of nanoparticles were then washed with 50% ethanolic solution to get rid of any unreacted reactants.

Nanoparticles thus formed are stabilized by morin itself which prevents the nanoparticles to agglomerate and also acts as a capping agent and prevents overgrowth of the nano- particles. It is worthy to mention that yield of γ-irradiated nanoparticles is more (~ 53 mg) compared to its non-irra- diated form (~ 38 mg) under the influence of high energy beam. This is mostly due to higher production of CuI due to higher reduction of Cu^{2+} to Cu^{+} in presence of the high energy beam that causes radiolysis in the medium containing morin generating larger free radicals and free electrons [29, 36, 48]. Nanoparticle solution sets A and B were prepared by adding ~ 1 mg of non-irradiated copper iodide nanoparticles (CuI-NP) and γ-irradiated (24 h) copper iodide nanoparticles (CuI-NP-γ) in 3 mL of water. Prior to each experiment, both the nanoparticle solutions were ultra-sonicated for 30 min at room temperature (25 ± 1 °C) for decent dispersion of the nanoparticles throughout the solution.

Characterization of nanoparticles

Both the nanoparticle solutions were first sonicated for 30 min at room temperature (25 ± 1 °C) and then centrifuged for 10 min at 2500 rpm to get the supernatant. A drop from each of the supernatant was then drop-casted on a carbon-coated copper grid. The grids were dried under IR lamp and were used to record the TEM micrographs to observe the structural morphologies like shape, size, dispersive nature and roughness of the synthesized nanoparticles. The same solutions were used to carry out the DLS experiment which determines the hydrodynamic radii of the NPs and gives an idea about the transient structure arising out of the Brownian motion of the molecules in fluid suspension. The solid NPs collected after washing and drying were used to perform experiments like PXRD, XPS and FTIR. A pinch of both types of solid nanoparticles was blended with dry KBr with the help of a mortar and pestle and a hydraulic press was used to make a KBr pellet of the sample. FTIR analysis of the NPs was done to know the presence of vibrational frequencies of the potential associations of the functional groups present in them. Again, solid powder sample of nanoparticle variants was placed in a grooved rectangular glass holder and PXRD analysis was carried out to find the crystallographic structure of the NPs. Both the NPs were further characterized by XPS in order to determine the elemental composition of the NPs and their corresponding chemical and electronic states.

Spectral sensing of CA 19-9 by the nanoparticle solutions

UV-Visible absorption spectroscopy was used in order to explore the biomarker sensing ability of both CuI-NP and CuI-NP-γ. For that, 2 mL of RL was used as a blank to perform all the experiments. As working medium, reconstituted serum, 1000-fold diluted in RL medium, was used for each set of experiment in order to keep the reaction conditions at per with biological significance. To this working medium, different known aliquots of CA 19-9 (5 U/mL) were spiked to the cuvette containing 2 mL of serum solution and the corresponding spectra were recorded at the λ_{max} 280 nm (owing to tyrosine residues in CA 19-9) as control [48, 49]. In order to get detectable absorption spectra, aliquots of 0.20 mL from each nanoparticle solution set (set A and B) were added to the cuvette containing 1.80 mL of the serum solu- tion. To these solutions, known aliquots of CA 19-9 (5 U/ mL) were gradually added with proper mixing and their sub- sequent absorbance were recorded at the λ_{max} 280 nm. Fur- ther simulations of different pathophysiological conditions with elevated levels of glucose, cholesterol, bilirubin and insulins were performed, where their concentrations were kept higher than normal physiological limits to mimic condi- tions like diabetes, hypercholesterolemia, hepatic disorder and hyperinsulinemia respectively. The individual effects were monitored which further corroborate CA 19-9 sensing ability of the NPs in presence of these biomolecules. For that, 0.02 mL each of 1 mM dextrose and cholesterol and 0.03 mL of 3 mM bilirubin were mixed with the serum solution and their respective absorbance spectra were monitored both in presence and absence of the nanoparticles (set A and B). Again, as pancreatic β-cells release insulin when glucose level increases in bloodstream, further simulations were car- ried out in presence of insulin to monitor its contribution towards CA 19-9 sensing by the NPs. Briefly, 0.002 mL (40 mIU/mL) each of actrapid and huminsulin were mixed with the serum medium and sensing assays were repeated. As there is a direct association between insulin and glucose, their combined effects were also monitored both in presence and absence of the nanoparticles (set A and B) by adding 0.002 mL (40 mIU/mL) actrapid or huminsulin and 0.02 mL (1 mM) dextrose in the working serum medium. The final spectra recorded were the average of three runs. Using this UV-Visible spectrophotometric method, limit of detection (LOD) and limit of quantification (LOQ) of CA 19-9 were calculated using the following equations with the help of slope (S) and standard deviation (σ) of the calibration curves of the responses.

$$LOD = 3.3(\sigma/S) \quad (1)$$

$$LOD = 10(\sigma/S) \quad (2)$$

where LOD is the lowest concentration of the analyte which can be detected and is greater than the uncertainty associated with it. LOQ is the lowest concentration of the analyte which can be quantitatively measured with acceptable precision and accuracy [12].

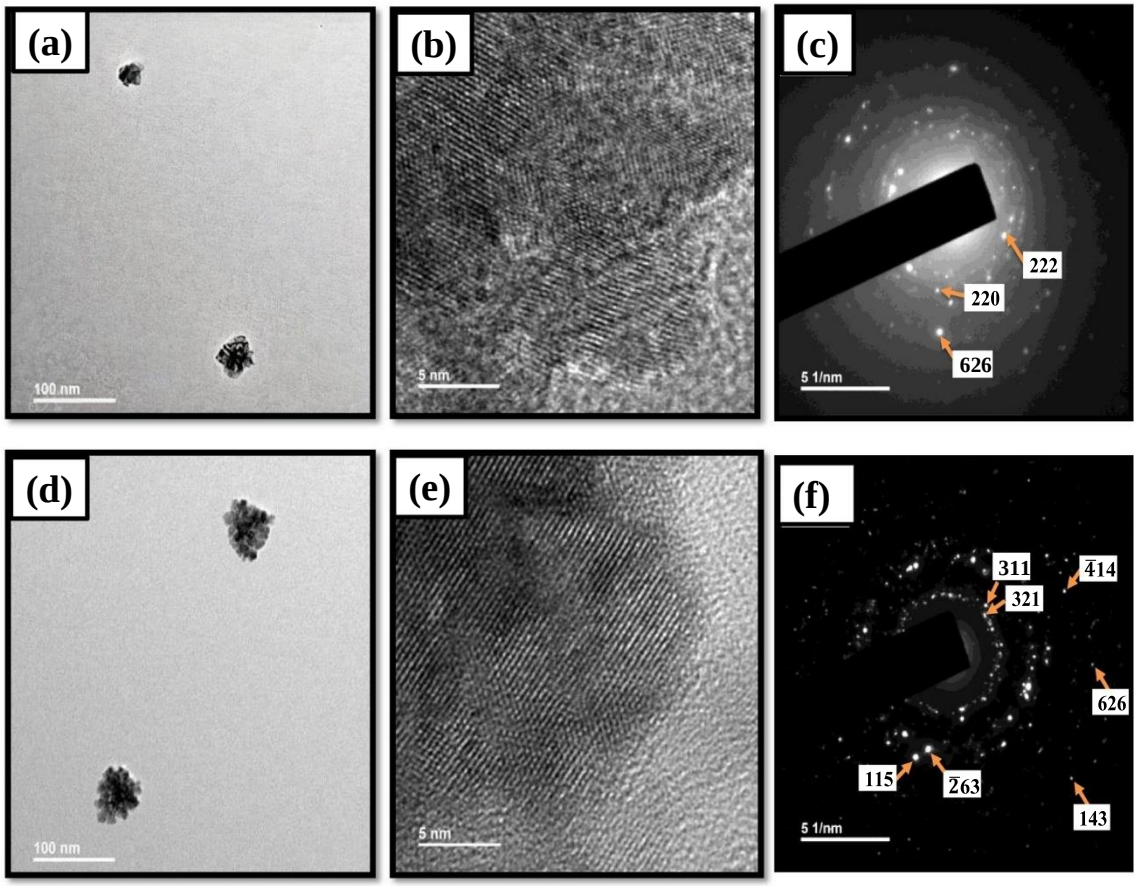

Fig. 1 For CuI-NP, **a** TEM image, **b** lattice fringes, **c** SAED pattern; For CuI-NP-γ, **d** TEM image, **e** lattice fringes, **f** SAED pattern

Fig. 2 Particle size distribution of **a** CuI-NP and **b** CuI-NP-γ

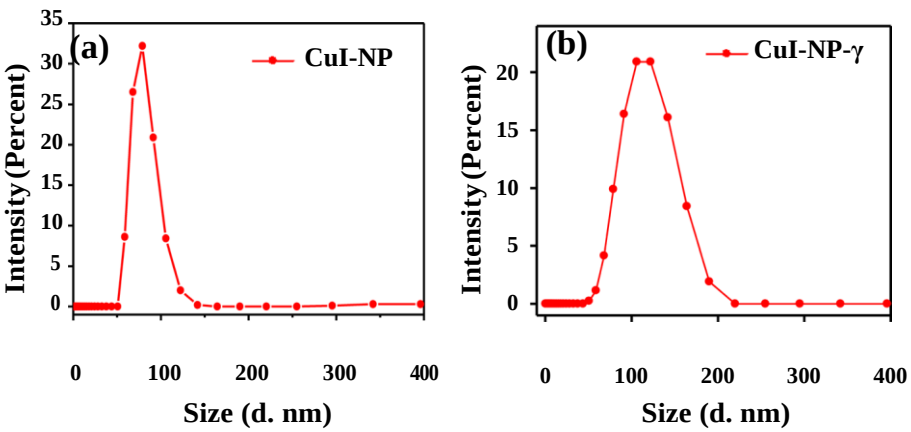

Spectroscopic studies for sensing mechanism

Fluorescence spectroscopy

Steady-state fluorescence experiments were performed using a spectrofluorometer with aquartz cuvette of 1 cm pathlength. The fluorescence intensity of CA 19-9 (5 U/ mL) excited at 295 nm keeping the slits with band passes at 5 nm for both excitation and emission channels was recorded at 25 °C. After that, small aliquots of the stock solution containing 0.15 mg/mL of CuI-NP-γ were added successively to CA 19-9 (5 U/mL). Working medium as explained earlier was used as reference blanks for each binding experiment. The quenching data of the fluorescence of CA 19-9 was analyzed to determine the binding dissociation constant (K_d) for the interaction between the

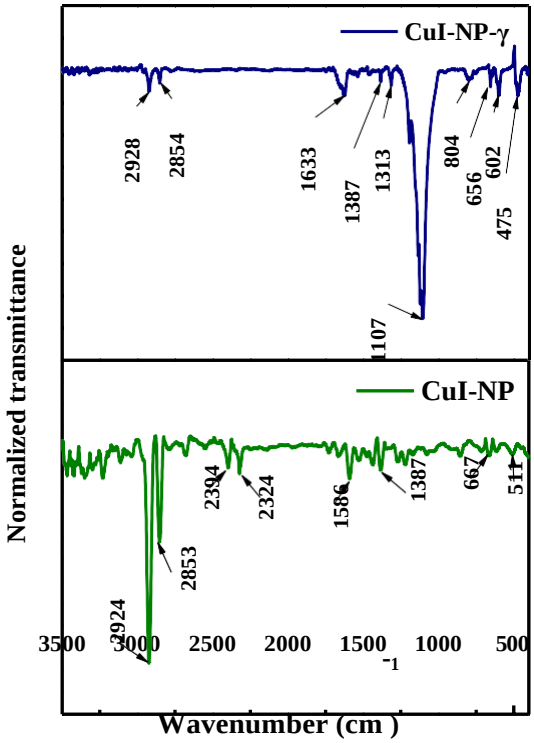

Fig. 3 FTIR spectra of CuI-NP (green) and CuI-NP-γ (blue). (Color figure online)

NPs and CA 19-9 both in absence and presence of high concentration of interfering molecules like glucose and cholesterol to mimic the pathophysiological disorders using the following equation [50].

$$1/\Delta F = 1/\Delta F_{max} + K_d/\Delta F_{max} \cdot C_p - C_0 \quad (3)$$

where ΔF and ΔF_{max} are the initial change in fluorescence intensity and the change in fluorescence intensity when the interaction between protein and the quencher reaches to the saturation phase, respectively. The concentration of NPs and the initial concentration of protein are referred to as Cp and C_0 respectively. The intercept of the plot of 1/ΔF versus 1/ (Cp – C_0) gives the value of ΔF_{max}.

Circular dichroism spectroscopy

Circular dichroism (CD) spectroscopy is a powerful and sensitive technique to elucidate the conformational changes in the native structure of proteins upon binding with nano- particles. Any alterations in secondary structure of proteins can be ascertained by monitoring the far-UV CD spectra of proteins which are highly sensitive towards protein struc- tures. CD spectra of CA 19-9 as well as other biomarkers CA 125 and CEA (biomarkers for ovarian and colorectal cancer respectively) were recorded both in presence and absence of CuI-NP-γ to study the selective interaction of the CuI-NP-γ towards CA 19-9 in serum medium. The CD spectra were taken in the range of 200–240 nm using a quartz cell of 1 mm path length. Final spectra were taken as the average of three runs. The CD results of the aforementioned proteins were expressed in terms of mean residual ellipticity (MRE) at 208 nm using the following equation [41]

$$[\&\beta] = \frac{\mu\theta}{10LC} \quad (4)$$

Table 1 FTIR data of CuI-NP and CuI-NP-γ

NPs	Wavenumber (cm^{-1})	Functional group	References
CuI-NP	2924, 2853	Rocking bending vibration of the $–CH_2$	[51]
	2394	–O–H stretching	[52]
	2324	–C=C of alkenes	[53]
	1586	–C=C (aromatic) stretching	[54]
	1387	–C–C–C of alkane	[55]
	667	–Cu–I	[33]
	511	–Cu–I	
CuI-NP-γ	2928, 2854	Rocking bending vibration of the $–CH_2$	[51]
	1633	–C=O stretching	
	1387	–C–C–C of alkane	[55]
	1313	–O–H bending	[56]
	1107	–C–O–C of ether	[57]
	804	–C–H stretching of aromatic ring	[58]
	656	–Cu–I	[33]
	602	–Cu–O stretching	[59]
	475	–Cu–I	[33]

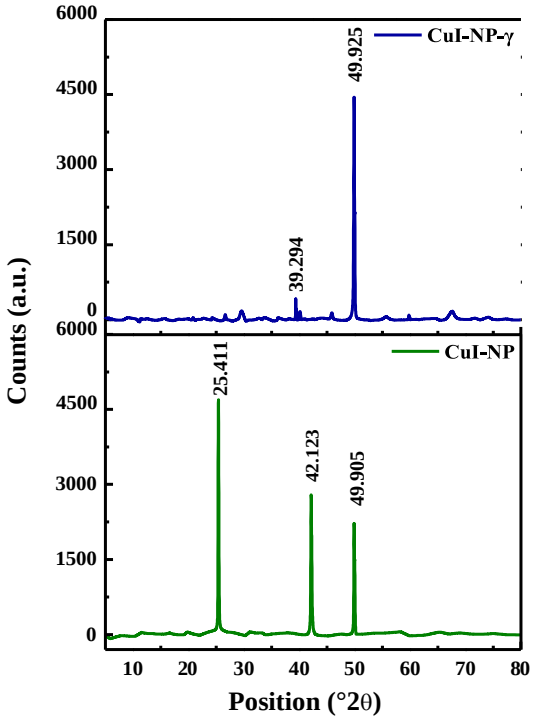

Fig. 4 PXRD patterns of CuI-NP (green) and CuI-NP-γ (blue). (Color figure online)

Where C is the micro-molar concentration of the proteins, L is the path length of the cuvette (0.1 cm), θ is the observed rotation and μ is the mean residual weight of the proteins. The α-helical contents of these proteins in presence and absence of CuI-NP-γ were calculated from MRE values at 208 nm using the following equation

$$\alpha - \text{helix}(\%) = \frac{[-\text{MRE}_{208} - 4000]}{[33000 - 4000]} \quad (5)$$

where MRE_{208} is the observed MRE value at 208 nm, 4000 is the MRE value of the *β*-form and random coil formation cross at 208 nm, 33,000 is the MRE value of pure α-helix at 208 nm.

Results and discussion

TEM analysis

TEM micrographs confirm the formation of spherical nanosized copper iodide nanoparticles. The nanoparti- cles have a porous texture with average particle size of 20–25 nm (Fig. 1a). A dark inner core covered by a lighter shade indicates that the metal iodide-NPs are coated by the organic layer of morin at the outer surface. Presence of lattice fringes in CuI-NP could be seen from Fig. 1b whereas Fig. 1c shows the SAED pattern of it which illustrates the crystalline structure of the CuI-NP. γ-irradiation retain the shape and texture of the nanoparticles with a slightly enhanced average size of CuI-NP-γ being 35–40 nm (Fig. 1d). CuI-NP-γ appears to be larger in size due to higher growth rate in presence of γ-radiation which is also supported by the following studies of DLS and PXRD. All other features viz., porous nature and presence of the organic layer at the outer surface remain similar to its non-irradiated counterpart. Figure 1e shows the lattice fringes present in CuI-NP-γ and its crystallographic nature could further be seen from its SAED pattern (Fig. 1f).

DLS study

Laser diffraction studies show particle size distribution of the nanoparticles where it could be seen that the average particle size of CuI-NP and CuI-NP-γ are 80 and 105 nm respectively (Fig. 2) which agrees with the TEM data. The larger particle size in DLS is due to the greater hydrodynamic radius of both the nanoparticles in solution. In the hydration environment, there is a gentle reorganization of the nanoparticles which accounts for the difference in size of TEM and DLS measurements.

FTIR analysis

The FTIR spectra of the prepared NPs are shown in Fig. 3 and their corresponding peaks are listed in Table 1. The sharp peaks at 2924, 2853 and 1387 cm^{-1} appear for the rocking, bending and stretching vibrations of CH_2 and C–C–C of alkane that arise from the changes in the morin structure upon interaction with CuI nanoparticles in the medium. However, the peaks at 2324, 1586 cm^{-1} also appear due to the alkene and aromatic groups present in unreacted morin. Small peaks at 667 and 511 cm^{-1} also appear due to Cu–I stretching vibrations. Upon 24 h of γ irradiation, there is a drastic structural modification on the NP surface caused by the high energy beam that results in the genera- tion of free radicals and rearrangement of chemical struc- ture. The morin attached at the surface of the NPs undergo a subtle structural modification which causes the peak intensities at 2924, 2853, 1387 cm^{-1} to diminish sharply. Whereas, a new intense peak appears at 1107 cm^{-1} arising out of the –C–O–C stretch of the ether present in morin. The carbonyl (–C=O) stretching of morin at 1633 cm^{-1} also becomes prominent due to this structural modification. The peaks at 667 and 511 cm^{-1} due to Cu-I stretching vibra- tions get shifted towards lower range at 656 and 475 cm^{-1} and become sharper due to structural rearrangement. Similar structural rearrangements with weakening and/or shifting of

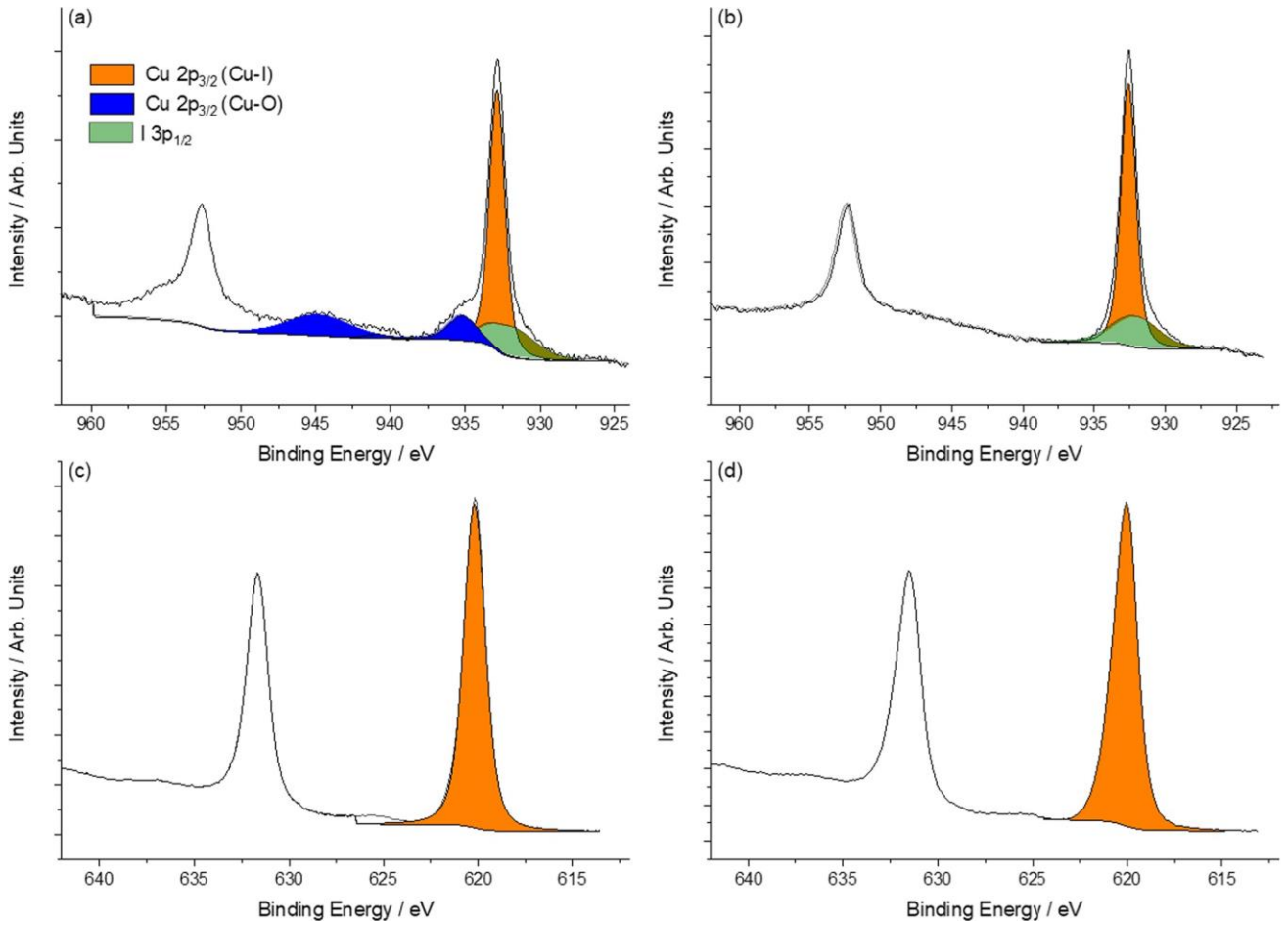

Fig. 5 Cu2p and I3d core-level XP spectra for (**a**, **c**) CuI-NP (**b**, **d**) for CuI-NP-γ. Orange coloration for both Cu and I show the integrated peaks for CuI, whilst the blue color shows the Cu(II) species. The green peak is the $I3p_{1/2}$ signal on which the $Cu2p_{3/2}$ peak is superimposed

Table 2 Limit of detection (LOD) values for CA 19-9 in different conditions obtained spectrophotometrically

Variants	LOD (U/mL)							
	Conditions*							
	N	D	C	B	A	H	A + D	H + D
CA-19-9	0.082 ± 0.004	0.096 ± 0.005	0.084 ± 0.004	0.233 ± 0.011	0.079 ± 0.004	0.076 ± 0.004	0.086 ± 0.004	0.134 ± 0.007
CA-19-9 + CuI-NP	0.062 ± 0.003	0.051 ± 0.002	0.048 ± 0.002	0.187 ± 0.009	0.073 ± 0.004	0.075 ± 0.004	0.080 ± 0.004	0.040 ± 0.002
CA-19-9 + CuI-NP-γ	0.066 ± 0.003	0.037 ± 0.002	0.034 ± 0.002	0.157 ± 0.008	0.034 ± 0.002	0.029 ± 0.001	0.049 ± 0.002	0.035 ± 0.002

Conditions*: *N* none, *D* dextrose, *C* cholesterol, *B* bilirubin, *A* actrapid, *H* huminsulin, *(A + D)* actrapid + dextrose, *(H + D)* huminsulin + dextrose

FTIR peaks have been observed for other nanoparticles like Ni-NP, Ru-NP upon γ-irradiation [36, 38].

PXRD analysis

Powder X-ray diffraction analysis was carried out to investigate the crystalline nature of the prepared nanoparticles. Fig- ure 4 shows the presence of well-defined peaks in the X-ray diffraction pattern which confirms the presence of periodic crystal lattice in both the nanoparticles. The peaks were then matched with the database obtained from the Joint Com- mittee on Powder Diffraction Standards (JCPDS). It could be seen that for CuI-NP, major diffraction came from 2θ values of 25.408º, 42.121º and 49.914º which correspond to (111), (220) and (311) planes respectively (Fig. 4). The lattice structure of CuI-NP is mostly face-centered with a

Table 3 Various analytical parameters for the spectrophotometric detection of CA 19-9 by NP

variants NPs	Parameters								
	Conditions	Regression equati	on Slope (S)	Intercep t (C)	R^2	Molar absorptivity (ε) ($mol^{-1} L cm^{-1}$)	Standard deviation (σ)	LOD (U/mL	) LOQ (U/mL)
CuI-NP	None	y = mx + C	0.119	0.0533	0.982	0.119×10^6	0.002	0.062	0.187
	Dextrose		0.155	0.103	0.988	0.155×10^6	0.002	0.051	0.385
	Cholesterol		0.124	0.0678	0.989	0.124×10^6	0.002	0.048	0.145
	Bilirubin		0.089	0.413	0.858	0.089×10^6	0.005	0.186	0.565
	Actrapid		0.152	0.097	0.975	0.152×10^6	0.003	0.073	0.221
	Huminsulin		0.074	0.048	0.974	0.074×10^6	0.001	0.075	0.226
CuI-NP-γ	None	y = mx + C	0.126	0.114	0.98	0.126×10^6	0.002	0.066	0.201
	Dextrose		0.134	0.055	0.993	0.134×10^6	0.001	0.037	0.113
	Cholesterol		0.125	0.077	0.995	0.125×10^6	0.001	0.034	0.102
	Bilirubin		0.080	0.435	0.895	0.080×10^6	0.004	0.157	0.476
	Actrapid		0.106	0.08	0.995	0.106×10^6	0.001	0.034	0.102
	Huminsulin		0.119	0.097	0.996	0.119×10^6	0.001	0.029	0.088

cubic system which matches well with the literature (JCPDS no. 82-2111) [23, 31–33]. Upon γ-irradiation, changes in lattice system of the nanoparticles are observed as several modifications in the diffraction patterns in CuI-NP along with appearance of new peaks. It might be due to the lattice strain induced on the system due to the high energy radia- tion as seen for other nanoparticles like Ag-NP [30]. Most intense diffraction in CuI-NP-γ comes from the 2θ value of 49.925º which corresponds to (626) plane which is also pre- sent in CuI-NP. It is worthy to mention that, copper iodide nanoparticles with higher purity FCC lattice were obtained using green synthesis approach as compared to the conven- tional chemical routes [22, 23]. Reports show that CuI-NP with hexagonal primitive lattice and sometimes mixture of hexagonal with triangular geometry are formed when wet chemical method, heat treatment, physical vapour deposi- tion were used [60–62]. The lattice of CuI-NP-γ is majorly primitive and orthorhombic.

XPS analysis

XPS analysis of both CuI-NP and CuI-NP-γ materials (Fig. 5) reveal a strong $I3d_{5/2}$ peak at 619.9 eV, however there are significant differences in the $Cu2p_{3/2}$ core-level spectra. The $Cu2p_{3/2}$ of the CuI-NP-γ material reveals a single Cu oxidation state with a $Cu2p_{3/2}$ binding energy of 932.6 eV, with a corresponding Auger parameter of 1848.4 eV (Cu LMM Auger, 915.8 eV), which is in good agreement with those expected for CuI [63]. However, it is well established that for Cu(I) compounds, final state effects arising from photoemission typically dominate especially with compounds which have a potential for significant polarization or electron mobility [64].

For the initial the CuI-NP material, two Cu species are evident, the first at 932.6 eV is attributed again to CuI, whilst the second is attributed to Cu(II), given the characteristic satellite structure between ca. 940 and 950 eV.

Analysis of the $Cu2p_{3/2}$ peak is slightly complicated by the overlapping $I3p_{1/2}$ peak (green peak in Fig. 5(a)), however fitting of this iodine peak gives an identical atomic concentration to that calculated for the $I3d_{5/2}$ peak suggesting good modelling of the underlying iodine peak. The ratio of I/Cu is 1.1, again in excellent agreement with the stoichiometry expected for CuI.

This result further validates that γ-irradiation generates higher number of free radicals and free solvated electrons in the medium by radiolysis which further helps in higher reduction of Cu^{2+} to Cu^{+} [29]. CA 19-9 is a tyrosine containing glycoprotein [39, 65] where its peptide structure has the tendency to agglomerate in presence of Cu^{2+} and binding of tyrosine with Cu^{2+} is weak [66]. This could be due to the fact that in Cu^{2+}-tyrosine system, there is no interac- tion between the metal cation and π-electron cloud of the aromatic ring in its ground state structure. Upon binding with Cu^{2+}, the amino acid gets oxidized and a repulsive electrostatic interaction is experienced between the aromatic ring of tyrosine and the metal cation [67]. In contrast, in Cu^{+}-tyrosine system ($\Delta G°_{298}$= 75.1 kcal/mol), the metal cation can interact with the π system of the amino acid and forms a more stable structure than that of in Cu^{2+}-tyrosine system ($\Delta G°_{298}$= 295.9 kcal/mol), which is also supported by their relative Gibbs free energy values [67]. Thus, CA 19-9 prefers to bind with CuI-NP-γ which contains Cu^{+} to

Table 4 Comparison between this designed method and other methods for CA 19-9 detection

Sl No.	Nano-material	Synthesis condition	Sensing method	Sensing medium	Linear range	LOD	Reference
1.	1D-MoS_2 NRs/$LiNb_3O_8$/AuNPs@POM	$HAuCl_4$, $H_3PMo_{12}O_{40}$, n-propanol, Dewar cell, Nb_2O_5, LiOH, autoclave, calcination, Na_2MoO_4, CH_3CSNH_2	Differential pulse voltammetry	PBS (pH 7.0)	0.1–10 μU/mL	0.030 μU/mL	[68]
2.	AuNPs	HAuCl4, Sodium citrate, boiling	Lateral flow strip biosensing	Human plasma in PBS (pH 7.4)	5–100 U/mL	5 U/mL	[69]
3.	Ni nanoclusters	$NiSO_4$, BSA, NaOH pH 12, 65 °C, dialysis	Fluorescence	PBS (pH 7.4)	1 pg/mL-48 ng/mL	0.13 pg/mL	[70]
4.	CQD/Au nanocomposite	Glucose, 120 °C, microwave oven, dialysis	Fluorescence	Human serum in PBS (pH 7.4)	0.01–350 U/mL	0.007 U/mL	[71]
5.	ZnO quantum dot	$Zn(CH_3COO)_2$, absolute ethanol, 80 °C, LiOH	Fluorescence, square wave voltammetry	PBS (pH 7.4)	1–180 U/ml and 0.1–180 U/ml	0.04 U/ml and 0.25 U/mL	[72]
6.	Dextran-Fe_3O_4 NPs/Graphene/CdTe quantum dot	$FeSO_4$, $FeCl_3$, N_2 flow, field, vacuum dry, graphene, EDC, NHS, DMF, Octa-Ammonium-POSS, NaOH, Cd^{2+}, NaHTe, L-Cysteine, oven dried at 65 °C	Electrochemiluminescence	Human serum, magnetically purified, high-gradient magnetic field, PBS (pH 7.0)	0.005–100 pg/mL	0.002 pg/mL	[73]
7.	Au nanotriangular arrays	Polystyrene sphere, silicon wafer, O_2 plasma, Mantis e-beam evaporation system	Fluorescence	PBS (pH 7.4)	1×10^{-6} U/mL^{-1} U/mL	7.7×10^{-7} U/mL	[74]
8.	Fe_3O_4 NPs coated carbon nanotube	MWCNTs, HCl, H_2SO_4, $FeCl_3$, $FeCl_2$, NH_3, pH 10	Lateral flow strip biosensing	Human whole blood in PBS (pH 7.4)	2-200 U/mL	30 U/mL	[75]
9.	Luminol-AgNPs@ZIF-67/g-C_3N_4@PtNPs	67/g-C_3N_4, Melamine, alumina crucible, 600 °C, HNO_3, $AgNO_3$, luminol, ZIF-67, H_2PtCl_6, sodium citrate, $NaBH_4$	Electrochemiluminescence	PBS (pH 7.4)	0.0001–10 U/mL	31 μU/mL	[76]
10.	Ag/g–C_3N_4	Melamine, alumina crucible, N_2 flow, HNO_3, reflux, vacuum dry, $AgNO_3$, 80 °C	Linear sweep voltammetry	Tris-HNO_3 buffer (pH 7.4)	5 mU/mL–50 U/mL	1.2 mU/mL	[77]
11.	CeO_2/FeO_x@mC_{500}	$Ce(NO_3)_3$, $Fe(NO_3)_3$, H_3BTC, oven dry, tube furnace, N_2 atmosphere, CeO_2	Electrochemical impedance spectroscopy	PBS buffer (pH 7.4)	0.1 mU/mL–10 U/mL	10 μU/mL	[78]

Table 4

Nano-material	Synthesis condition	Sensing method	Sensing medium	Linear range	LOD	Reference
PtRu nanoassemblies/ AuNS/BSA/Ab2	Octylphenoxypolyethoxyethanol (NP-40)/triethylene glycol/Pt(acac)2 or Ru(acac)3	Electrochemical immunosensing	–	10^{-4}–70^{-4} U/mL	3.3×10^{-5} U/ mL	[79]
TiS_3 nanoribbon	1-Naphthylamine (NA)/ glutaraldehyde (GA)/ monoclonal antibody 19-9	FET immunosensing	–	–	1.3×10^{-13} U/mL	[80]
MoS_2	MoS_2 crystal/ H_2O_2/ H_2SO_4/DMF/ 1-naphthylamine	FET immunosensing	Human serum	–	2.8×10–13 U/mL	[81]
AuNP	Gold film, trimethoxysilane	Localized surface plasmon resonance (LSPR) UV–Visible spectroscopy	Human serum	–	0.0001 U/mL	[82]
γ-Irradiated CuI-NP	$CuSO_4$, KI, morin hydrate, γ-irradiation		Synthetic serum	–	0.029 U/mL	This study

a great extent compared to CuI-NP containing both the Cu^{+} and Cu^{2+} which is also reflected from the LOD data reported below.

Spectral sensing of CA 19-9 by the nanoparticle solutions

Interaction between the NPs and CA 19-9 was monitored spectrophotometrically at the wavelength 280 nm. As control experiment, absorption intensities were as measured which increases upon gradual addition of CA 19-9 to the cuvette containing serum solution. Similar change is observed in presence of the physiological variables, i.e., dextrose, cho- lesterol, bilirubin, actrapid and huminsulin in the serum medium. In the actual experiment, increase in absorption was also recorded when the said simulations were performed in presence of NPs, with a much higher rate. Table 2 shows calculated LOD values of each condition set. It could be seen that CuI-NP-γ is able to sense CA 19-9 to a superior extent as compared to CuI-NP. Due to the charged nature and higher surface activity of the γ-irradiated particles, they could deliver higher signal enhancement and thereby offer higher sensitivity.

Nonetheless, in presence of various physiological variables like dextrose, cholesterol, bilirubin, actrapid and huminsulin, LOD value of CA 19-9 further rises substantially in control solutions. This may cause difficulties in timely detection of CA 19-9 in serum. But results show that their presence does not interfere with CA 19-9 sensing by the NPs. In fact, significant improvement in detection threshold was achieved in serum medium in presence of glucose, cholesterol, bilirubin, actrapid and huminsulin as the LOD obtained are much less as compared to an otherwise healthy condition (Figs. S1–S24). Thus, this detection method could also be applied efficiently to the patients having these comorbidities. However, even if the patient serum sample does not contain any of these physiochemical entities, CA 19-9 sensing could still be accomplished efficiently by the NPs by the external addition of them in patient serum. Table 3 shows different analytical parameters associated with CA 19-9 sensing by the NPs along with their correlation coefficient (R^2). Compared to different reported methods for CA 19-9 sensing using nanomaterials (Table 4), this proposed method is hassle-free and devoid of complex synthesis procedure of nanoparticles to achieve good sensitivity towards CA 19-9.

Mechanism of sensing

Fluorescence spectral analysis

The increase in sensitivity of the detection of CA 19-9 by CuI-NP-γ in presence of high concentration of biomolecules

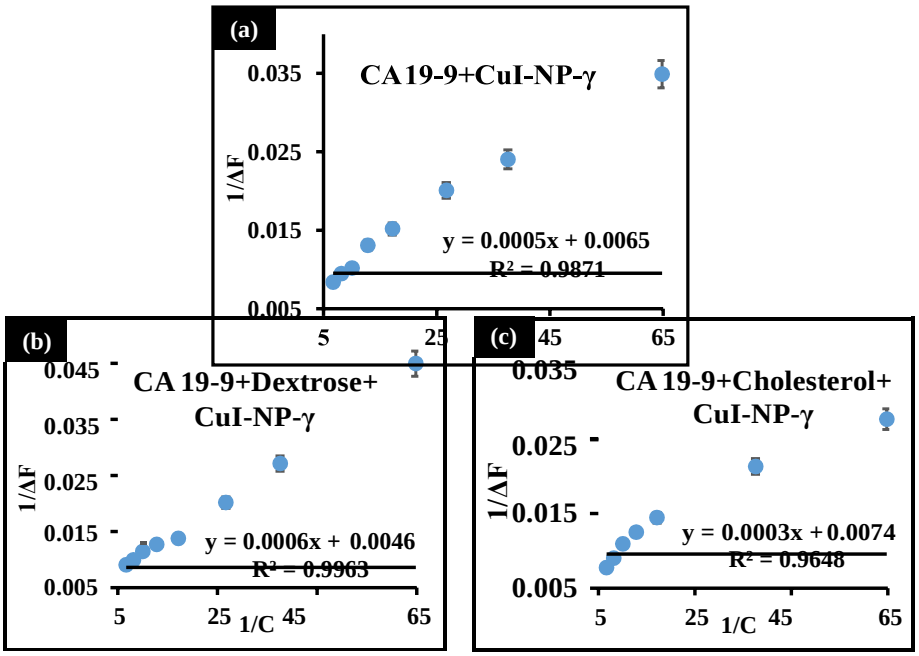

Fig. 6 1/ΔF versus 1/C plot of different condition sets of interaction between CA 19-9 and CuI-NP-γ

Table 5 Different binding dissociation constant associated with inter- action between CA 19-9 and CuI-NP-γ at 25 ºC

Binding constant, K_d (μM)	Conditions		
	None	Dextrose	Cholesterol
CA 19-9+CuI-NP-γ	76.9	130.43	40.54

like glucose, cholesterol, bilirubin, insulin, etc., indicates interactions of the NPs with these entities. Hence, the inter- actions of the protein biomarker with the NPs in serum medium were investigated by fluorescence spectroscopy both in presence and absence of glucose and cholesterol to determine the effect of these molecules on the values of binding dissociation constant of the interactions (Figs. S25–S27). Figure 5a–c shows the corresponding plot of 1/

ΔF versus 1/C. From Table 5 it is evident that the binding dissociation constant values are in comparable range. Although presence of cholesterol increased the binding affinity of the NPs towards CA 19-9 to some extent as the value of binding dissociation constant decreased. CA 19-9 being a cell adhesion glycoprotein resides on cell membrane and it may have interaction with other cell membrane components like cholesterol. Hence, the interaction between NP and CA 19-9 gets more stabilized in presence of cholesterol leading to lower value of binding dissociation constant. On the contrary, addition of external glucose molecule in the reaction mixture containing CA 19-9, the tetra-saccharide antigen, perturbs the interaction between NPs and CA 19-9 which may be due to the repulsive force between the carbohydrate molecules [39, 67, 68]. However, the binding dissociation constant values for the interaction between NPs and CA 19-9 in presence of bilirubin and insulin could not be evaluated as the intrinsic fluorescence intensity of CA 19-9 got quenched in presence of bilirubin while the fluorescence of insulin itself interfered with the analysis (Fig. 6).

Table 7 Limit of detection (LOD) values for CA-125

Variants	Limit of detection (LOD) (U/mL)		
	Conditions		
	None (N)	Dextrose (D)	Cholesterol (C)
CA-125	0.044±0.002	0.035±0.002	0.056±0.003
CA-125+CuI-NP	0.050±0.002	0.084±0.004	0.078±0.004
CA-125+CuI-NP-γ	0.077±0.004	0.043±0.002	0.064±0.003

Table 6 α-Helix (%) of the proteins at different conditions

	CA 19-9+ Serum	CA 19-9+ Serum + CuI-NP-γ	CA 125+ Serum	CA 125+ Serum + CuI-NP-γ	CEA+ Serum	CEA+ Serum +CuI-NP-γ
α-helix (%)	63.56	60.92	35.0	52.62	22.96	41.1

Table 8 Limit of detection (LOD) values for CEA

Variants	Limit of detection (LOD) (ng/mL)		
	Conditions		
	None (N)	Dextrose (D)	Cholesterol (C)
CEA	0.006 ± 0.0003	0.014 ± 0.0007	0.030 ± 0.001
CEA+CuI-NP	0.019 ± 0.0009	0.028±0.001	0.036±0.002
CEA+CuI-NP-γ	0.021±0.001	0.036±0.002	0.033±0.002

Circular dichroism spectral analysis

CD spectra of all the proteins (CA 19-9, CA 125, and CEA) show two negative bands in the UV region at 208 and 222 nm which are the characteristics of the α-helix rich second- ary structure of the proteins (both due to n π^* transition of α-helix peptide bond). CD spectroscopy reveals that peak positions in CA 19-9 spectra remains unaltered upon binding with CuI-NP-γ which remains predominantly α-helical in nature. Figure S28 shows that for CA 19-9, the change in the band intensity of its CD spectra upon binding with CuI-NP-γ were not that much significant, which suggests that native conformation of the protein remains somewhat undisturbed as the extent of decrease in α-helical content is small (from
63.56 to 60.92%). The decrease in α-helical content (less than 5% reduction of α-helicity) of CA 19-9 in presence of CuI-NP-γ indicates that the NPs bind with amino acid residues of the main polypeptide chain and forms protein-NP (CA 19-9-CuI-NP-γ) complex [69]. However, upon addition of CuI-NP-γ to CA 125 and CEA, band intensity of their corresponding CD spectra decreased to a greater extent. From the calculated percentage α-helicity content of these proteins both in presence and absence of CuI-NP-γ (Table 6), it is evident that α-helicity content increases sharply for CA 125 (from 35.0 to 52.62%) and CEA (from 22.96 to 41.10%) in presence of CuI-NP-γ. This suggests that binding of CuI-NP-γ with both CA 125 and CEA causes perturbation in the native conforma- tion of these proteins by altering their secondary structures which results in partial unfolding and loosening of the protein integrity [69]. At this condition, sensing of CA 125 and CEA by CuI-NP-γ might not be possible which also agrees with the UV-Visible spectroscopic data.

Specificity of the designed method

To confirm the specificity of the developed method, synthesized NPs were also used to sense CA-125 and CEA in serum by keeping all the experimental conditions alike (S29-S46). However, the NPs failed to sense both the biomarkers at any physiological circumstances (Tables 7 and 8). The NPs could not lower the LOD values of these biomarkers below their control values in any of the conditions. This verifies that the NPs have good specificity in sensing CA 19-9 and there could be not as much of chance for a false positive result.

Conclusion

The present work proposes a simple, fast, green and cost-effective method for superior in vitro detection of cancer biomarker CA 19-9. The synthesis procedure does not involve use of costly or hazardous raw materials or complex experimental conditions like use of N_2 atmosphere, magnetic field, O_2 plasma, prolonged synthesis time, etc. This study is a novel method for the detection of CA 19-9 in presence of several common physiological parameters that give rise to comorbidities like, diabetes, hypercholesterolemia, hepatic disorder, hyperinsulinemia, etc. The results indicate that the LOD value for CA 19-9 is lower with the γ-irradiated NPs and even lower in presence of biomolecules that cause physiological disorders. The lowest LOD value was observed for huminsulin and actrapid (0.029 ± 0.001 U/mL and 0.034 ± 0.002 U/mL respectively). Thus serum samples from patients suffering from these comorbidities will show even more sensitive detection of CA 19-9. However, even if the patient serum is free from these biomolecules, CA 19-9 sensing could still be enhanced efficiently by the nanoparticles upon their in vitro addition to serum samples. The interactions between the NPs and the biomarker protein were confirmed using fluorescence and circular dichroism spec- troscopy. This property of CuI nanoparticles has revealed a new field for the optical sensing of cancer biomarkers.

Supplementary Information The online version contains supplemen- tary material available at https://doi.org/10.1007/s10967-023-09056-3.

Acknowledgements KS and SB express sincere thanks to UGC-DAE-CSR, Collaborative Research Scheme no. UGC-DAE-CSR/KC/CRS/19/RC07/0982/1017 for providing necessary funding. SB acknowledges UGC-DAE-CSR, Govt. of India for providing fellow- ship. DD acknowledges the award and funding of CSIR SRA B12827. We express our sincere thanks to Dr. Aparna Datta, UGC-DAE Consortium for Scientific Research, Kolkata, India, for obtaining FTIR and fluorescence data. We thank DST FIST (SR/FST/CS-II/2017/27(C) dated 29.09.2018) and CAS-V (UGC) (540/3/CASV/2015 (SAP-I) for funding the PXRD instrument and UV-Vis spectrophotometer respectively

Declarations

Conflict of interest Authors declare no conflict of interest.

References

1. Wolfgang CL, Herman JM, Laheru DA, Klein AP, Erdek MA, Fishman EK, Hruban RH (2013) Recent progress in pancreatic cancer. CA Cancer J Clin 63:318–348

2. Siegel RL, Miller KD, Jemal A (2019) Cancer statistics, 2019. CA Cancer J Clin 69:7–34
3. Jawad ZAR, Theodorou IG, Jiao LR, Xie F (2017) Highly sen- sitive plasmonic detection of the pancreatic cancer biomarker CA19-9. Sci Rep 7:1–7
4. Huang Z, Jiang Z, Zhao C, Han W, Lin L, Liu A, Weng S, Lin X (2017) Simple and effective label-free electrochemical immuno- assay for carbohydrate antigen 19 – 9 based on polythionine-Au composites as enhanced sensing signals for detecting different clinical samples. Int J Nanomed 12:3049–3058
5. Xu X, Xiao Y, Hong B, Hao B, Qian Y (2019) Combined detec- tion of CA19-9 and B7-H4 in the diagnosis and prognosis of pancreatic cancer. Cancer Biomark 25:251–257
6. Wu E, Zhou S, Bhat K, Ma Q (2013) CA 19 – 9 and pancreatic cancer. Clin Adv Hematol Oncol 11:53–55
7. Passerini R, Cassatella MC, Boveri S, Salvatici M, Radice D, Zorzino L, Galli C, Sandri MT (2012) The Pitfalls of CA19-9: routine testing and comparison of two automated Immunoassays in a reference Oncology Center. Am J Clin Path 138:281–287
8. Duffy MJ (1998) CA 19-9 as a marker for gastrointestinal cancers: a review. Ann Clin Biochem 35:364–370
9. Zhu H, Fan GC, Abdel-Halim ES, Zhang JR, Zhu JJ (2016) Ultrasensitive photoelectrochemical immunoassay for CA19-9 detection based on CdSe@ZnS quantum dots sensitized TiO_2NWs/ Au hybrid structure amplified by quenching effect of $Ab_2@V^{2+}$ conjugates. Biosens Bioelectron 77:339–346
10. Park IJ, Choi GS, Jun SH (2009) Prognostic value of serum tumor antigen CA 19-9 after curative resection of colorectal cancer. Anticancer Res 29:4303–4308
11. Singh M, Singh S, Prasad S, Gambhir IS (2008) Nanotechnology in medicine and antibacterial effect of silver nanoparticles. Dig J Nanomater Biostruct 3:115–122
12. Xavier SSJ, Karthikeyan C, Kim AR, Yoo DJ (2014) Colorimetric detection of melamine using β-cyclodextrin-functionalized silver nanoparticles. Anal Methods 6:8165–8172
13. Korde P, Ghotekar S, Pagar T, Pansambal S, Oza R, Mane D (2020) Plant extract assisted eco-benevolent synthesis of selenium nanoparticles-a review on plant parts involved, characterization and their recent applications. J Chem Rev 2:157–168
14. Khurana A, Tekula S, Saifi MA, Venkatesh P, Godugu C (2019) Therapeutic applications of selenium nanoparticles. Biomed Pharmacother 111:802–812
15. Cao Y, Mo G, Feng J, He X, Tang L, Yu C, Deng B (2018) Based on ZnSe quantum dots labeling and single particle mode ICP-MS coupled with sandwich magnetic immunoassay for the detection of carcinoembryonic antigen in human serum. Anal Chim Acta 1028:22–31
16. Feraoun H, Aourag H, Certier M (2003) Theoretical studies of substoichiometric CuI Mater. Chem Phys 82:597–601
17. Naoomi Y, Ryuichiro I, Yoshihiko N (2016) Truly transparent p-type γ -CuI thin films with high hole mobility. Chem Mater 28:4971–4981
18. Perera VPS, Tennakone K (2003) Recombination processes in dye-sensitized solid-state solar cells with CuI as the hole collector. Sol Energy Mat Sol Cells 79:249–255
19. Yang M, Xu JZ, Xu S, Zhu JJ, Chen HY (2004) Preparation of porous spherical CuI nanoparticles. Inorg Chem Commun 7:628–630
20. Sreedhar B, Arundhathi R, Reddy PL, Kantam ML (2009) CuI nanoparticles for C–N and C–O cross coupling of hetero- cyclic amines and phenols with chlorobenzenes. J Org Chem 74:7951–7954
21. Tornoe CW, Christensen C, Meldal M (2002) Peptidotriazoles on solid phase: [1,2,3]-triazoles by regiospecific copper(I)-catalyzed 1,3-dipolar cycloadditions of terminal alkynes to azides. J Org Chem 67:3057–3064
22. Vijayakumar A, Rajagopal R (2016) Green synthesis and characterisation of copper (I) iodide nanoparticles using kidney bean seed extract and its anti-bacterial activity. Int J Sci Eng Res 7:602–609
23. Fernandez AC, Archana KM, Rajagopal R (2020) Green synthesis, characterization, catalytic and antibacterial studies of copper iodide nanoparticles synthesized using *Brassica oleracea var capitata f rubra* extract. Chem Data Coll 29:100538
24. Akai TIA, Karasawa T, Kojima K, Komatsu T (2000) Exciton transitions in the hexagonal CuI microcrystallites grown on polymers. J Lumin 87:516–518
25. Tennakone K, Kumara GRRA, Kottegoda IRM, Perera VPS, Aponsu GMLP, Wijayantha KGU (1998) Deposition of thin conducting flms of CuI on glass. Sol Energy Mater Sol Cells 55:283–289
26. Liu Y, Zhan J, Zeng J, Qian Y, Tang K, Yu W (2001) Ethanolther- mal synthesis to γ-CuI nanocrystals at low temperature. J Mater Sci Lett 20:1865–1867
27. Penner RM (2003) Hybrid electrochemical/chemical synthesis of quantum dots. Acc Chem Res 33:78
28. Sirimanne PM, Soga T, Jimbo T (2003) Identification of various luminescence centers in CuI films by cathodoluminescence technique. J Luminesc 105:105–109
29. Abdelghany AM, Abdelrazek EM, Badr SI, Abdel-Aziz MS, Morsi MA (2017) Effect of Gamma-irradiation on biosynthe- sized gold nanoparticles using Chenopodium murale leaf extract. J Saudi Chem Soc 21:528–537
30. Ansari Z, Dhara S, Bandyopadhyay B, Saha A, Sen K (2016) Spectral anion sensing and γ-radiation induced magnetic modifications of polyphenol generated Ag-nanoparticles. Spectrochim Acta A Mol Biomol Spectrosc 156:98–104
31. Tavakoli F, Salavati-Niasari M, Mohandes F (2013) Green synthesis of flower-like CuI microstructures composed of trigonal nanostructures using pomegranate juice. Mater Lett 100:133–136
32. Phetcharat P, Sangsanoh P, Choipang C, Chaiarwut S, Suwantong O, Chuysinuan P, Supaphol P (2023) Curative effects of copper Iodide embedded on gallic acid incorporated in a poly (vinyl alcohol)(PVA) liquid bandage. Gels 9(1):53
33. Archana KM, Yogalakshmi D, Rajagopal R (2019) Application of green synthesized nanocrystalline CuI in the removal of aqueous mn (VII) and cr (VI) ions. SN Appl Sci 1:522
34. Indubala E, Dhanasekar M, Sudha V, Malar EP, Divya P, Sherine J, Rajagopal R, Bhat SV, Harinipriya S (2018) L-Alanine cap- ping of ZnO nanorods: increased carrier concentration in ZnO/ CuI heterojunction diode. RSC Adv 8(10):5350–5361
35. Pérez-Alvarez M, Cadenas-Pliego G, Pérez-Camacho O, Comparán-Padilla VE, Cabello-Alvarado CJ, Saucedo-Salazar E (2021) Green synthesis of copper nanoparticles using cotton. Polymers 13(12):1906
36. Singh P, Ansari Z, Ray S, Bandyopadhyay B, Sen K (2020) Effect of γ-irradiation on ruthenium-morin nanocomposite for trace detection of ce(IV), Ce(III) and Dy(III). Mater Chem Phys 248:122949
37. Panhwar QK, Memon S (2014) Synthesis of Cr (III)-morin complex: characterization and antioxidant study. Sci World J, 2014
38. Ansari Z, Bhattacharya TS, Saha A, Sen K (2019) γ-Irradiated Ni-hesperidin nanocomposite for selective trace-level sensing of sulfide ions. J Radioanal Nucl Chem 322:79–88
39. Ansari Z, Sarkar K, Saha A, Singha A, Sen K (2016) Enhanced anion sensing by γ-irradiated polyphenol capped iron oxide nanoparticles. J Radioanal Nucl Chem 308:517–525
40. Lavanya N, Anithaa AC, Sekar C, Asokan K, Bonavita A, Donato N, Leonardi SG, Neri G (2017) Effect of gamma irradiation on

structural, electrical and gas sensing properties of tungsten oxide nanoparticles. J Alloys Compd 693:366–372
41. Qindeel R (2017) Effect of gamma radiation on morphological and optical properties of ZnO nanopowder. Results Phys 7:807–809
42. Zhang H, Wang M, Chen L, Liu Y, Liu H, Huo H, Sun L, Ren X, Deng Y, Qi A (2017) Structure-solubility relationships and thermodynamic aspects of solubility of some flavonoids in the solvents modeling biological media. J Mol Liq 225:439–445
43. Abbad S, Wang C, Waddad AY, Lv H, Zhou J (2015) Prepara- tion, in vitro and in vivo evaluation of polymeric nanoparticles based on hyaluronic acid- poly (butyl cyanoacrylate) and D-alpha-tocopheryl polyethylene glycol 1000 succinate for tumor-targeted delivery of morin hydrate. Int J Nanomed 10:305–320
44. Waddad AY, Abbad S, Yu F, Munyendo WLL, Wang J, Lv H, Zhou J (2013) Formulation, characterization and pharmacokinet- ics of Morin hydrate niosomes prepared from various non-ionic surfactants. Int J Pharm 456:446–458
45. Gopal JV (2013) Morin Hydrate: botanical origin, pharmacological activity and its applications: a mini-review. Pharmacogn J 5:123–126
46. Fairley N, Fernandez V, Richard-Plouet M, Guillot-Deudon C, Walton J, Smith E, Flahaut D, Greiner M, Biesinger M, Tougaard S, Morgan D, Baltrusaitis J (2021) Systematic and collaborative approach to problem solving using X-ray photoelectron spectroscopy. Appl Surf Sci 5:100112
47. Vu DKN, Nguyen DKV (2021) Gamma irradiation-assisted synthesis of silver nanoparticle-embedded graphene oxide-TiO_2 nanotube nanocomposite for organic dye photodegradation. J Nanomater 2021:1–14
48. Klug TL, LeDonne NC, Greber TF, Zurawski VR (1988) Purifica- tion and composition of a novel gastrointestinal tumor-associated glycoprotein expressing sialylated lacto-N-fucopentaose II (CA 19-9). Cancer Res 48:1505–1511
49. Castaño C, Vignoni M, Vicendo P, Oliveros E, Thomas AH (2016) Degradation of tyrosine and tryptophan residues of peptides by type I photosensitized oxidation. J Photochem Photobiol B Biol 164:226–235
50. Das D, Sen K (2021) Effect of organo-selenium anticancer drugs on nitrite induced methemoglobinemia: a spectroscopic study. Spectrochim Acta A Mol Biomol Spectrosc 245:118946
51. Sanches NB, Pedro R, Diniz MF, Mattos EDC, Cassu SN, Dutra RDCL (2013) Infrared spectroscopy applied to materials used as thermal insulation and coatings. J Aerosp Technol Manag 5:421–430
52. Yang C, Lin K, Chang J (2015) A simple way to synthesize 3D hierarchical HAp porous microspheres with sustained drug release. Ceram Int 41:11153–11160
53. Maria MFF, Ikhmal WMKWM, Amirah MNNS, Manja SM, Syaizwadi SM, Chan KS, Sabri MGM, Adnan A (2019) Green approach in anti-corrosion coating by using Andrographis paniculata leaves extract as additives of stainless steel 316L in seawater. Int J Corros Scale Inhib 8:644–658
54. Trivedi M, Branton A, Trivedi D, Shettigar H, Bairwa K, Jana S (2015) Fourier transform infrared and ultraviolet-visible spectroscopic characterization of biofield treated salicylic acid and sparfloxacin. Nat Prod Chem Res 5
55. Ortiz E, Solis H, Noreña L, Loera-Serna S (2017) Degradation of red anthraquinone dyes: alizarin, alizarin S and alizarin complex- one by ozonation. Int J Environ Sci Dev 8:255
56. Liu X, Liu Z, Wang L, Zhang S, Zhang H (2017) Preparation and performance of composite films based on 2-(2-aminoethoxy) ethyl chitosan and cellulose. RSC Adv 7:13707–13713
57. Rohatgi CV, Dutta NK, Choudhury NR (2015) Separator membrane from crosslinked poly (Vinyl Alcohol) and poly (methyl vinyl ether-alt-maleic anhydride). Nanomaterials 5:398–414
58. Chandran A, Mary S, Varghese HT, Panicker CY, Manojkumar TK, Alsenoy CV, Rajendran G (2012) Vibrational spectroscopic study of (E)-4-(benzylideneamino)-N-carbamimidoyl benzenesulfonamide. Int Sch Res Notices 2012
59. Panhwar QK, Memon S, Bhanger MI (2010) Synthesis, characterization, spectroscopic and antioxidation studies of Cu (II)–morin complex. J Mol Struct 967:47–53
60. Yao K, Chen P, Zhang Z, Li J, Ai R, Ma H, Zhao B, Sun G, Wu R, Tang X, Li B, Hu J, Duan X, Duan X (2018) Synthesis of ultrathin two-dimensional nanosheets and van der Waals heterostructures from non-layered γ-CuI. npj 2D Mater Appl 2(1):16
61. Akopyan IK, Golubkov VV, Dyatlova OA, Mamaev AN, Novikov BV, Tsagan-Mandzhiev AN (2010) Specific features of the CuI nanocrystal structure in photochromic glasses. Phys Solid State 52:805–809
62. Myeni N, Ghosh SK, Perla VK, Mallick K (2019) Copper iodide nanoparticles within the organic matrix: an efficient catalyst for the electro-oxidation of formic acid. Mater Res Express 6(10):1050a7
63. Biesinger MC (2017) Advanced analysis of copper X-ray photoelectron spectra. Surf Interface Anal 49:1325–1334
64. Moretti G (2013) The Wagner plot and the Auger parameter as tools to separate initial-and final-state contributions in X-ray photoemission spectroscopy. Surf Sci 618:3–11
65. Wu E, Zhou S, Bhat K, Ma Q (2013) CA 19-9 and pancreatic cancer. Clin Adv Hematol Oncol 11:53
66. Alghamdi A, Wellbrock T, Birch DJ, Vyshemirsky V, Rolinski OJ (2019) Cu^{2+} effects on beta-amyloid oligomerisation moni- tored by the fluorescence of intrinsic tyrosine. Chem Phys Chem 20:3181–3185
67. Rimola A, Rodríguez-Santiago L, Sodupe M (2006) Cation – π interactions and oxidative effects on Cu^{+} and Cu^{2+} binding to phe, tyr, trp, and his amino acids in the gas phase insights from first-principles calculations. J Phys Chem B 110:24189–24199
68. Yola ML, Atar N (2021) Carbohydrate antigen 19-9 electrochemical immunosensor based on 1D-MoS_2 nanorods/$LiNb_3O_8$ and polyoxometalate-incorporated gold nanoparticles. Microchem J 170:106643
69. Baryeh K, Takalkar S, Lund M, Liu G (2017) Development of quantitative immunochromatographic assay for rapid and sensitive detection of carbohydrate antigen 19-9 (CA 19-9) in human plasma. J Pharm Biomed Anal 146:285–291
70. Bahari D, Babamiri B, Salimi A (2020) An eco-friendly MIP- solid surface fluorescence immunosensor for detection of CA 19-9 tumor marker using ni nanocluster as an emitter labels. J Iran Chem Soc 17:2283–2291
71. Alarfaj NA, El-Tohamy MF, Oraby HF (2018) CA 19-9 pancreatic tumor marker fluorescence immunosensing detection via immobilized carbon quantum dots conjugated gold nanocomposite. Int J Mol Sci 19:1162
72. Gu B, Xu C, Yang C, Liu S, Wang M (2011) ZnO quantum dot labeled immunosensor for carbohydrate antigen 19-9. Biosens Bioelectron 26:2720–2723
73. Gan N, Zhou J, Xiong P, Li T, Jiang S, Cao Y, Jiang Q (2013) An ultrasensitive electrochemiluminescence immunoassay for carbohydrate antigen 19-9 in serum based on antibody labeled Fe_3O_4 nanoparticles as capture probes and graphene/CdTe quantum dot bionanoconjugates as signal amplifiers. Int J Mol Sci 14:10397–10411
74. Jawad ZA, Theodorou IG, Jiao LR, Xie F (2017) Highly sensitive plasmonic detection of the pancreatic cancer biomarker CA 19-9. Sci Rep 7:1–7
75. Huang Y, Wen Y, Baryeh K, Takalkar S, Lund M, Zhang X, Liu G (2017) Lateral flow assay for carbohydrate antigen 19–9 in whole blood by using magnetized carbon nanotubes. Microchim Acta 184:4287–4294

76. Mo G, He X, Qin D, Meng S, Wu Y, Deng B (2021) Spatially-resolved dual-potential sandwich electrochemiluminescence immunosensor for the simultaneous determination of carbohydrate antigen 19–9 and carbohydrate antigen 24-2. Biosens Bioelectron 178:113024
77. Sun AL, Qi QA (2016) Silver-functionalized g-C_3N_4 nanohybrids as signal-transduction tags for electrochemical immunoassay of human carbohydrate antigen 19-9. Analyst 141:4366–4372
78. Wang M, Hu M, Hu B, Guo C, Song Y, Jia Q, He L, Zhang Z, Fang S (2019) Bimetallic cerium and ferric oxides nanoparticles embedded within mesoporous carbon matrix: electrochemical immunosensor for sensitive detection of carbohydrate antigen 19-9. Biosens Bioelectron 135:22–29
79. Tan YY, Sun HN, Liu M, Liu A, Li SS (2022) Simple synthesis of PtRu nanoassemblies as signal amplifiers for electrochemical immunoassay of carbohydrate antigen 19–9. Bioelectrochemistry 148:108263
80. Rahmani H, Majd SM, Salimi A (2022) Highly sensitive and selective detection of the pancreatic cancer biomarker CA 19 – 9 with the electrolyte-gated MoS_2-based field-effect transistor immunosensor. Res Sq
81. Rahmani H, Majd SM, Salimi A, Ghasemi F (2023) Ultrasensi- tive immunosensor for monitoring of CA 19-9 pancreatic cancer marker using electrolyte-gated TiS_3 nanoribbons field-effect transistor. Talanta 257:124336
82. Sharifi M, Khalilzadeh B, Bayat F, Isildak I, Tajalli H (2023) Application of thermal annealing-assisted gold nanoparticles for ultrasensitive diagnosis of pancreatic cancer using localized surface plasmon resonance. Microchem J 190:108698